

Ionic transport in spontaneously ion-intercalated van der Waals layered structures

Ata Utku Özkan,^{*,†,¶} T. Serkan Kasırga,^{*,‡,¶} and Aykut Erbaş^{*,†,¶}

[†]*Institute of Materials Science and Nanotechnology, Bilkent University, Ankara 06800, Turkiye*

[‡]*Department of Physics, Middle East Technical University, Ankara 06800, Turkiye*

[¶]*Bilkent National Nanotechnology Research Center - UNAM, Ankara 06800, Turkiye*

E-mail: utku.ozkan@bilkent.edu.tr; kasirga@unam.bilkent.edu.tr;
aykut.erbas@unam.bilkent.edu.tr

Abstract

Understanding ionic transport under strong confinement is crucial for the design of next-generation energy, catalytic, and information-processing materials; however, repeated field-driven ion motion often degrades conventional solid electrolytes. Van der Waals layered materials offer an alternative by providing structurally resilient ion-transport channels, yet the microscopic origins of their non-equilibrium transport behavior remain poorly understood. Here, we investigate field-driven ionic conduction in sodium-intercalated layered MnO_2 as a model self-intercalated van der Waals solid, using all-atom nonequilibrium molecular dynamics simulations that explicitly capture ion–water correlations and layer morphology. We demonstrate that ionic conductivity depends nonlinearly on the applied electric field, interlayer spacing, water content, and lattice flexibility. The applied electric field induces spatial segregation of water, coupled to distortions of the MnO_2 sheets, producing coexisting regions populated by highly hydrated and weakly hydrated ions with suppressed conductivity. Concurrently, ionic

transport exhibits a non-monotonic dependence on the total amount of intercalated water, with boundary domains of weakly hydrated ions displaying relatively higher mobility. In fluctuation-free layers, ion transport transitions from single-particle motion to a collective conduction regime characterized by elongated, same-charge ionic clusters that violate Nernst–Einstein behavior. Together, these findings provide a molecular-level mechanism linking confinement-induced electrostatic correlations and structural response to the emergent nonlinear transport observed experimentally in ion-intercalated MnO_2 , and suggest general design principles for robust, water-assisted ionic conductors.

Introduction

The transport of ionic charge and mass in solid media underpins a broad range of phenomena and technologies, including catalysis, energy storage, bioinspired information processing, and solid-state switching applications.^{1–5} However, repeated cyclic displacement of guest ions driven by external fields often induces structural degradation of the host material, ultimately limiting device stability and lifetime.^{6,7} Van der Waals (vdW) layered materials⁸ offer a promising alternative by providing well-defined interlamellar spaces that act as open ion-transport channels. In these systems, ions can migrate between confining layers without permanently disrupting the host lattice.^{9–12} Despite the wide availability of two-dimensional (2D) vdW materials capable of accommodating guest ions, post-synthetic ion intercalation is typically a slow and kinetically limited process, adding significant complexity to device fabrication and integration.^{13,14}

A potential solution to this challenge is the use of intrinsically ion-intercalated vdW materials, in which mobile ions are integral structural components of the crystal lattice and therefore do not require post-intercalation. In such systems, electrostatic charge balance between the surface atoms and oppositely charged interlayer ions stabilizes the structure while simultaneously permitting ionic motion under extreme confinement (i.e., sub-nanometer length

scales).¹⁵ Crucially, these ion-intercalated vdW materials are fundamentally distinct from nanoconfined electrolytes, where both counterions and co-ions coexist in confinement (e.g., between graphene layers),^{16–18} allowing the partial employment of bulk electrolyte theories.⁵ Yet, in ion-intercalating vdW solids, where mobile ions move within the electrostatic confinement of constrained surface charges, the governing physical principles of ionic transport remain largely unknown.

A model system that exemplifies intrinsically ion-intercalated vdW solids is the layered polymorph of MnO_2 (manganese oxide). These structures can host guest alkali ions (e.g., sodium, Na, or potassium, K) together with water molecules, intrinsically intercalated during synthesis, and thus provide a well-defined platform for studying ionic transport across vdW-confined layers.^{15,19–21} In recently synthesized single-crystalline MnO_2 , the mixed valence states of manganese within the layers ensure overall charge neutrality, rendering the interlayer alkali ions (Na^+ or K^+) the sole mobile charged species.²² In addition, ambient moisture is readily absorbed into the interlayer spacing, creating a confined, water-mediated environment between the ion-intercalated vdW layers.¹⁵ This unique combination of strong electrostatic confinement, structural order, and nanoscale hydration distinguishes layered MnO_2 from conventional nanoconfined electrolytes and makes it an ideal system for probing the fundamental mechanisms of ionic transport in intrinsically ion-intercalated layers.

While extensive data exist on the structural characterization and electrochemical performance of various ion-intercalated MnO_2 structures,^{23–26} quantitatively linking their underlying electrolyte chemistry to key performance metrics—such as ionic conductivity and capacitance—remains a significant challenge.^{27–29} Previous computational studies of MnO_2 sheets have shown that, in the absence of an external electric field, the equilibrium structure is governed by a subtle interplay between interlamellar water, ionic distributions, and the charge distribution within the manganese oxide layers.^{30,31} In practical device operation, however, external electric fields are inevitably applied to drive ionic transport. Electrical biases can induce transient or even permanent rearrangements of water molecules and inter-

calated ions confined within the interlayer spacing.¹⁹ Such field-driven effects, can in turn, trigger structural modifications of the ion-intercalated layers, which can give rise to nontrivial changes in activation energies and two-dimensional ionic mobilities.^{32–38} Consistent with this picture, studies on polycrystalline birnessite have identified intercalated water as the primary mediator of capacitive behavior, while spatially inhomogeneous ion distributions are found to promote local distortions of the MnO₂ sheet structure.^{19,39}

In experimental studies on single-crystalline, ion-intercalated MnO₂ sheets, we previously measured ionic conductivity in vacuum under various voltage biases.^{15,19} These studies demonstrated that externally applied in-plane electric fields mobilize intercalated ions and induce a peculiar, field-driven structural phase transition, accompanied by pronounced hysteresis in the current-voltage characteristics. In samples where ions were confined within layers of approximately $d_z \approx 7$ Å inter-layer spacing, the formation of water-rich and water-poor macroscopic regions was observed at voltage biases below ~ 0.01 V. Notably, water-poor regions exhibited weak ionic conductivity despite the presence of ions, suggesting a key role for water in the non-equilibrium motion of confined ions. However, experimental techniques cannot resolve the individual dynamical responses of cations, water molecules, and the host lattice, leaving the origin of the observed spatially inhomogeneous conductivity unresolved.

Non-equilibrium molecular dynamics (NEMD) simulations have demonstrated that ionic conductivity in electrolyte solutions confined between graphene layers can deviate significantly from ideal behavior when electrostatic correlations between oppositely charged ion pairs are altered under extreme (sub-nanometer) confinement.^{5,16,40} Under applied electric fields, ion transport can violate the Nernst–Einstein relation and lead to the formation of elongated, polyampholyte-like transient assemblies.⁵ Moreover, a reduction in the effective repulsion between ions of the same charge can further enhance conductivity.⁴¹ In analogy with ion transport in intercalated MnO₂ layers, such field-induced changes in electrostatic correlations, ion–water interactions, and layer morphology are likely to generate non-trivial current–voltage responses.

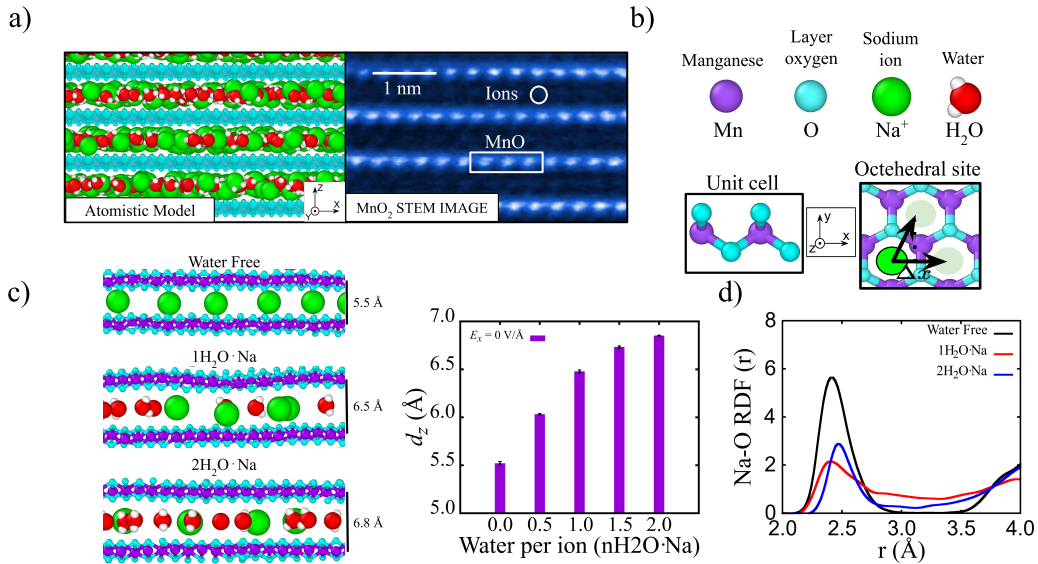


Figure 1: Modeling of single-crystalline MnO₂ layered structures (a) Representative MD snapshot and experimental image of a single-crystalline MnO₂ layer from the lateral (\hat{y}) direction. The experimental system is composed of 4 to 5 atomic layers.¹⁵ The simulated model is constructed by stacking 4 MnO₂ sheets in the \hat{z} direction. b) The atoms constituting the layers, including intercalated water and ions, are given in their vdW description. The unit lattice and Octahedral site of the MnO₂ surfaces are given with the same color codes. c) Lateral view of the layers for various water levels and inter-layer thickness averaged over equilibrium (field-free) simulation trajectories. d) Sodium-layer oxygen (Na-O) radial distribution functions of electric-field-free cases for various water levels.

Here, to elucidate the mechanisms of field-driven ionic transport in intrinsically intercalated van der Waals layers, we use sodium-intercalated MnO₂ sheets under external voltage bias as a model system and perform all-atom NEMD simulations that allow for morphological deformation of the confining layers. Our calculations indicate that ionic conductivity is strongly influenced by the interlayer spacing, water concentration, and layer-morphology effects. We observe nonlinear ionic conduction under applied fields, accompanied by bending distortions of the MnO₂ sheets. Furthermore, the electric field drives the segregation of water molecules, which leads to the formation of water-rich, ion-hydrated domains alongside water-depleted regions, both of which suppress overall conductivity.

Methodology

Simulation details

In molecular dynamics (MD) simulations, all atoms composing the system, including water molecules, ions, and the MnO_2 layer, are modeled explicitly. The MnO_2 sheets are prepared with replication of MnO_2 unit cell in all directions based on the experimentally reported lattice parameters (Figure 1a).⁴² A single unit cell is first replicated in the lateral (i.e., \hat{x} and \hat{y}) directions to obtain a single $\text{Mn}_{900}\text{O}_{1800} + \text{Na}_{225}^+$ nanosheet. Following, these sheets are stacked in the \hat{z} direction to obtain a total of 4 layers. The layers are periodic in the lateral directions, and there is no structural irregularity between neighboring sheets. The layers at the top and bottom also confine ions to satisfy the periodicity in the \hat{z} direction (Figure 1b). The dimensions of the simulation box are $86.8 \times 75.2 \times 28.0 \text{ \AA}^3$.

The pairwise interaction parameters between all atoms are defined *via* the CLAYFF forcefield.^{43,44} In this forcefield, the MnO_2 structure is stabilized by non-bonded interactions. Monovalent sodium ions are chosen to model cations in accordance with the previous experiments.^{15,19} For Mn atoms constituting the sheets, an atomic charge of $q_{\text{Mn}} = +3.75e$, where e is the elementary charge, is used to satisfy the mixed valence model of Mn^{+4} and Mn^{+3} valencies, upon modification of Lennard-Jones (LJ) pair coefficients.⁴⁵ Surface oxygen atoms also carry partial charges (Supplementary Table 1), and together with ions, they charge-neutralize the overall structure. The total number of Na^+ ions is fixed in all simulations. The short-range electrostatics between charged species are calculated via a cutoff distance of 10 \AA while the long-range electrostatics is calculated via the particle-particle particle-mesh method with an accuracy of 1.0e-4.⁴⁶ The SPC-E water model is used in all simulations and added randomly in between the sheets at prescribed concentrations. Intrinsic water intramolecular bond lengths and bond angles are constrained to fixed values using the SHAKE algorithm in LAMMPS, eliminating high-frequency vibrational modes while preserving correct translational and rotational.⁴⁷ These concentrations are referred to as n

$\text{H}_2\text{O}\cdot\text{Na}$, where n is the number of water molecules per ion and changes between $n = 0$ and $n = 3$ throughout this work. The software package Packmol is used to design the layered surfaces filled with the prescribed amount of water molecules, which are initially randomly distributed.⁴⁸

All simulations are run at a constant temperature T and a constant number N of atoms ensemble. In simulations, where the surface atoms are thermalized, a constant pressure P ensemble (i.e., NPT) is used to allow surface fluctuations. In NPT calculations, the pressure is set to $P = 1$ atm in all directions by keeping the simulation box angles constant by using an anisotropic barostat.⁴⁹ In simulations, where the inter-layer distance is fixed, the total volume of the simulation box V is preserved to satisfy the NVT conditions. In NVT simulations, the inter-sheet distance d_z is set to values ranging between $6.4 \leq d_z \leq 7.4 \text{ \AA}$, and only ions and water molecules are allowed to move under the Nose-Hoover thermostat.^{50,51}

In the equilibration simulations preceding the application of the external electric field, ions and water molecules are energy minimized. Following this, regardless of the production ensemble used, an equilibration procedure is applied at $T = 300$ K with a damping constant of 100 fs and a time step of $\Delta t = 1$ fs for 20 ns. All data-production runs are performed for up to 100 ns with the same time step Δt and temperature- and pressure-damping parameters under a constant electric field E_x applied in the \hat{x} direction (Figure 1b). The thermostat is applied only after excluding the center-of-mass movement contributions of the electric field. The maximum strength of the applied electric field is chosen such that the system temperature is maintained at the prescribed value by the thermostat throughout the simulation.

Calculation of ionic conductivity

In order to characterize the ionic current under external electric fields, we calculate the average current from the current density j as

$$I_x = j A_{xy}, \quad (1)$$

where the $j = Nq\langle v_x \rangle / A_{xy}d_z$, $q = +1e$ is the charge of a monovalent sodium ion, $\langle v_x \rangle$ is the time and ensemble averaged velocity of all ions in the \hat{x} direction, A_{xy} is the cross-sectional area of the interlayer channel, and N_c is the number of ions in the simulation box. Average interlayer spacing d_z is calculated from the difference between the mean Mn positions of the two adjacent layers averaged over all layer pairs, and the error bars are the mean of the per-layer variances. The velocity calculations are performed by calculating the slope of the displacement data for the last 20 ns of each 100-ns-long simulation trajectory. The interlayer distance in *NPT* simulations is obtained by averaging the vertical positions of all Mn atoms of each sheet and subtracting the mean values of adjacent layers. The standard errors are calculated and not shown if error bars are smaller than the symbol size.

In order to calculate the steady-state average ionic velocity, ionic displacement averaged over all ions is fitted with a function

$$\langle \Delta x \rangle = (1 - \exp(-t/\tau)) + \langle v_x \rangle t. \quad (2)$$

where τ defines a relaxation timescale, above which a linear increase in the displacement data is observed. The exponential term in Eq. 2 captures the rapid (i.e., ~ 15 ns) response of the layer and molecular distributions to the electric field, while the second term describes the linear growth with a slope equivalent to the average drift velocity of ions at longer times (i.e., $t \gg \tau$).

Results and Discussion

Electric field bias alters water distribution across the vdW layers

Inhomogeneous water distributions across MnO_2 vdW layers give rise to pronounced morphological distortions of the host lattice, manifested as spatial bending fluctuations and alterations in the thickness of the interlayer spacing.³¹ Consistent with these structural

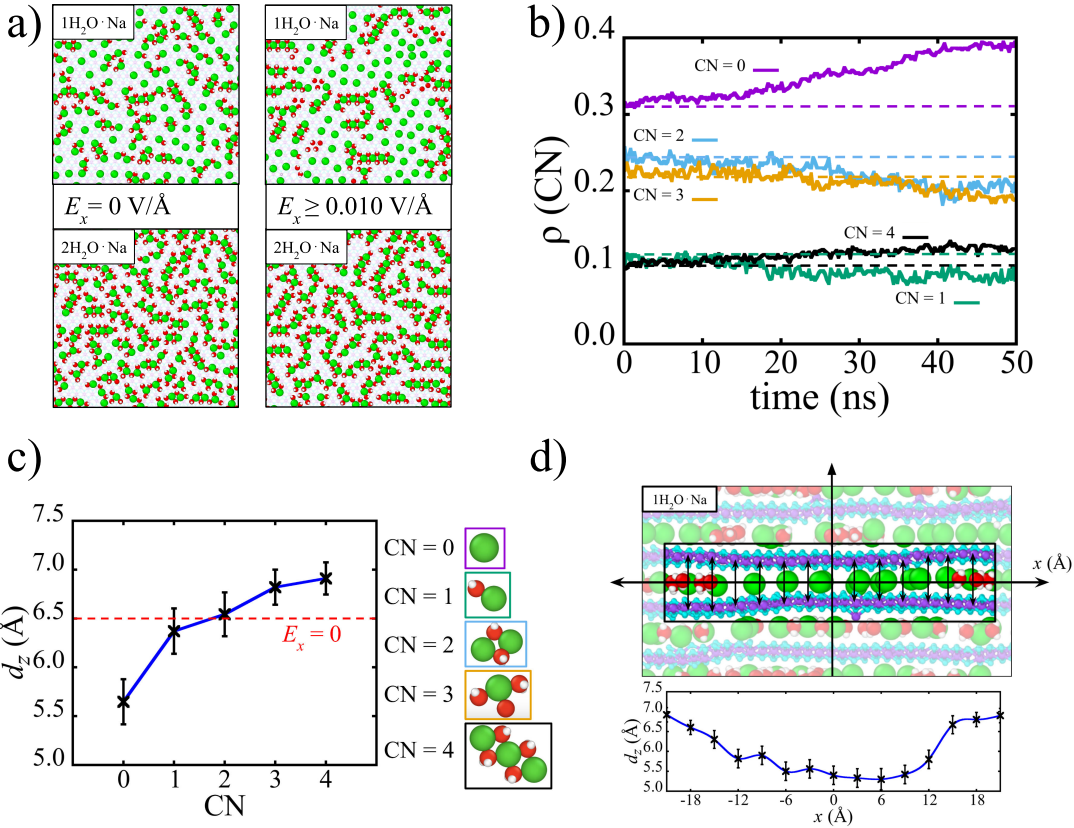


Figure 2: Effect of electric field and water segregation and layer morphology: a) Representative simulation snapshots for various water levels at the beginning and after 50 ns under an applied electric field. b) The fractions of ions with various coordination number (CN), which defines the number of water molecules in the first hydration shell as a function of time at $E_x = 0.02 \text{ V/}\text{\AA}$ for one water per ion case (i.e., $1\text{H}_2\text{O}\cdot\text{Na}$ water level). c) Average interlayer distance vs CN for $1\text{H}_2\text{O}\cdot\text{Na}$. d) A snapshot demonstrating the undulations in the interlayer height and corresponding layer thickness after 50 ns at $E_x = 0.02 \text{ V/}\text{\AA}$.

changes, experimental conductivity measurements reveal the coexistence of water-rich and water-poor domains under voltage bias, with significantly altered ionic mobility in less hydrated regions.^{15,19} To directly probe the microscopic origin of this coupling between ionic hydration, morphology, and transport, we simulated layered MnO₂ sheets both in the absence and presence of water under external electric-field biases. These simulations explicitly account for the intermingled effects of ion and water distributions, as well as the morphological response of the nanosheets to these distributions. We examine water-free systems as well

as systems with controlled water concentrations using non-equilibrium atomistic molecular dynamics simulations.

We first investigate the surface morphology of MnO_2 layers at varying levels of intercalated water, which can be experimentally controlled by vaporizing water at elevated temperatures.¹⁵ To achieve this, we randomly distributed the ions and water molecules across the layers and equilibrated the ionic positions for a minimum of 20 ns. In the absence of water, MnO_2 sheets maintains their structural stability and form layers with an average interlayer spacing of $d_z \approx 5.5 \pm 0.2 \text{ \AA}$, consistent with previous reports^{19,52,53} (Figure 1 and Supplementary Figure S1). Notably, a fraction of Mn atoms diffuse toward the interlayer region, however this doesn't affect the overall stability within time window of our simulations.⁵⁴

Next, a prescribed number of water molecules per ion is introduced between the MnO_2 nanosheets (Figure 1). Upon water intercalation, the average interlayer spacing increases markedly from $d_z \approx 5.5 \text{ \AA}$ to a water-concentration-dependent thickness (Figure 1c). This expansion arises primarily from the screening of electrostatic attraction between the intercalated ions and the oppositely charged surface atoms by water molecules³⁹ (Figure 1d). The spatial distributions of water molecules and ions remain homogeneous over equilibrium simulations extending up to 20 ns in the absence of an external electric field, resulting in a uniform interlayer thickness across the sheets (Figure 1 and Supplementary Figure S1). Further increases in the water content beyond approximately 2 water molecules per ion lead to additional interlayer swelling¹⁶ (Supplementary Figure S1).

While water-intercalated vdW MnO_2 layers are structurally stable and exhibit a uniform interlayer spacing at zero electric field, the application of an in-plane electric field alters the coupled distributions of water molecules and sodium ions. Under non-equilibrium conditions, the field drives a lateral redistribution of both species, leading to the spontaneous formation of distinct nanoscale water-rich and water-poor domains across the sheets (Figure 2a-b). This domain formation is most pronounced when the average hydration level is low, specifically when fewer than approximately two water molecules per ion are present, leaving a

significant fraction of octahedral sites locally devoid of water, and progressively weakens at higher water concentrations (Figure 2a).

To quantify this effect, we characterize the local hydration environment using the 2D equivalent of Na–O coordination number (CN), where $\text{CN} \approx 4$ corresponds to 4 water molecules near the first hydration shell of the ion (Figure 2b-c). This analyses reveals that while $\text{CN} = 0$ and 4 (i.e., unhydrated and fully hydrated ions increase), other hydration levels decreases upon the application of external field (Figure 2b).

The emergence of water–poor regions (with unhydrated ions) has a direct morphological effect on the host layer. Because water molecules screen the electrostatic attraction between intercalated sodium ions and the oppositely charged MnO_2 layers,³⁹ local solvent depletion strengthens ion–layer interactions. This enhanced attraction pulls the layers closer together, producing spatially varying interlayer distances and pronounced bending distortions of the sheets. As a result, the interlayer spacing becomes explicitly dependent on the local hydration state (Figure c-d). For instance, at a hydration level of one water molecule per ion, the average interlayer distance decreases to $d_z = 6.2 \pm 0.3 \text{ \AA}$ due to reduced water-mediated screening in solvent-poor domains (Figure 2c-d and Supplementary Figure S2).

Notably, once established, these hydration-driven structural inhomogeneities persist even after the external electric field is removed. The system does not spontaneously re-homogenize within the accessible simulation time window, indicating either an effectively irreversible transition or a relaxation process that is slow compared to ion and water diffusion. As the hydration level is further reduced, the solvent-poor regions expand monotonically, and the interlayer spacing approaches the value observed in fully dehydrated layers, namely $d_z \approx 5.5 \text{ \AA}$ (Supplementary Figure S3). To confirm that solvent segregation alone is sufficient to generate the observed structural distortions, we performed control simulations in which water molecules were initially distributed non-uniformly in the absence of an electric field (Supplementary Figure S2). These simulations reproduce the same hydration-dependent interlayer spacing and sheet distortions, demonstrating that the morphological response of the MnO_2

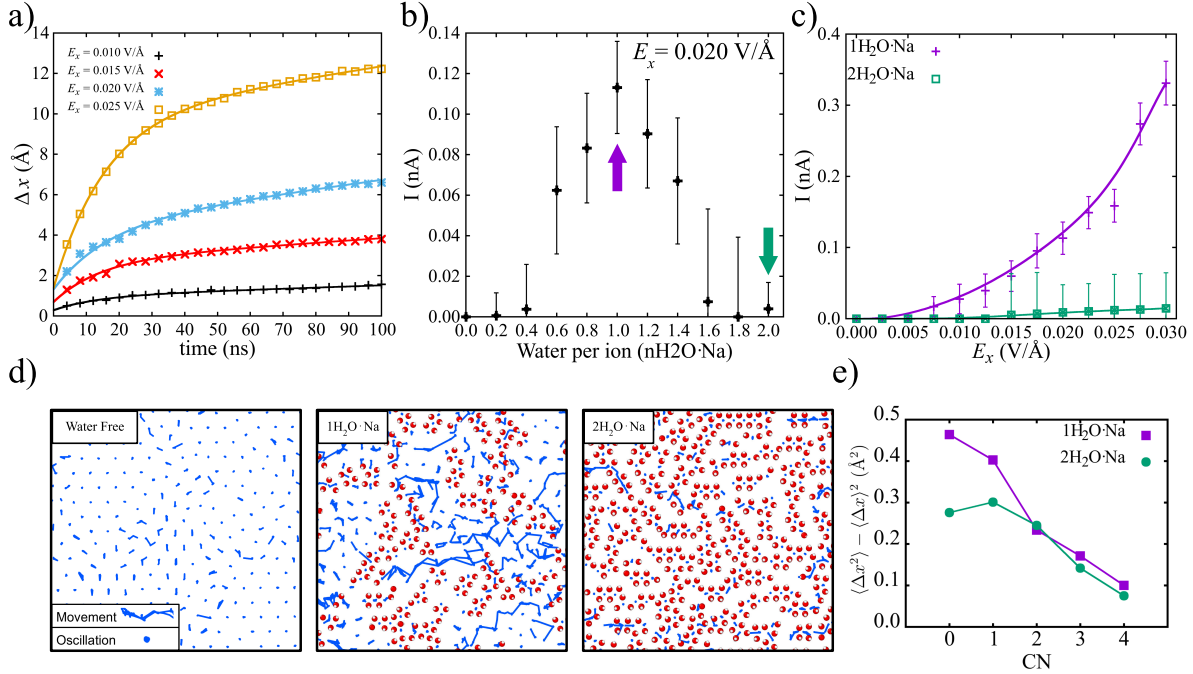


Figure 3: Water segregation versus ionic conduction: a) The displacement trajectories averaged over all ions for the $1\text{H}_2\text{O-Na}$ system for various electric field strengths. b) The ionic current as a function of water levels at $E_x = 0.02$ V/Å. c) Electric field versus current for one and two water per ions cases, which correspond to the highest- and lowest-conducting systems in (b). d) Visualization of ionic trajectories for MnO₂ layers intercalated by various levels of water calculated at the steady state regime between 50 ns–100 ns interval of the simulation; blue lines denote the path of a single ion and blue dots refer to no motion. e) Coordination number vs. expected value of square of ionic displacement calculated over 1-ns-time windows for various water levels at $E_x = 0.02$ V/Å.

layers is primarily governed by the local hydration rather than the electric field directly. Overall, our simulations demonstrate that voltage biases can induce water segregation, thereby affecting the interlayer thickness. As we will discuss next, this alteration can impact ionic movement across the MnO₂ vdW layers.

Ionic motion is modulated by local hydration

We reason that the field-driven segregation of water into the domains with hydrated and unhydrated ionic across the vdW MnO₂ layers can have a direct and measurable impact on ionic transport dynamics (Figure 3). This expectation is consistent with voltage-sweep

experiments, which show that above ~ 400 K—where intercalated water desorbs from the MnO_2 single-crystal layers, and the pronounced current-voltage hysteresis observed at lower temperatures disappears.¹⁵ This behavior suggests a transition to a transport regime in which ionic conduction is strongly suppressed in the absence of interlayer water.

Our simulations directly reproduce this water-dependent transition. In fully dehydrated MnO_2 layers, ions exhibit only initial displacement hops of less than ~ 1 Å, even under electric field strengths as high as $E_x = 0.05$ V/Å (i.e., comparable to the strengths to which water can break down). No sustained long-time ion motion is observed, resulting in effectively vanishing ionic conduction (Supplementary Figure S3). This suppression reflects the combined effects of reduced interlayer spacing, enhanced ion-layer electrostatic attraction, and the absence of water-mediated screening.

By contrast, gradual intercalation of water into the layers expands the interlayer spacing and lowers the electrostatic barriers for ion motion, enabling field-assisted ionic transport (Figures 2 and 3). For hydrated layers, the average ionic displacement exhibits a characteristic two-stage temporal behavior: an initial exponential increase during the first ~ 15 ns, followed by a linear growth regime at longer times. The crossover between these regimes coincides with the timescale over which water segregation develops within the layers (Supplementary Table 2). This indicates that the steady-state transport response emerges only after solvent redistribution is established in an electric-field strength-dependent manner.

Steady-state ionic currents, extracted from the linear long-time displacement regime (see Methods), increase sub-linearly with applied electric field strength (Figures 3). This deviation from Ohmic behavior indicates a field-dependent modification of ionic correlations and transport pathways, reminiscent of prior observations of non-Nernst-Einstein transport in confined electrolytes.^{5,41}

Because intercalated water simultaneously controls electrostatic screening and interlayer spacing, we next examine the dependence of ionic conductivity on hydration level (Figure 3). Surprisingly, the conductivity exhibits a non-monotonic dependence on water content:

both low (i.e., 0.2 water molecules per ion) and high (i.e., water molecules per ion) water levels in our simulations lead to minimal ionic mobility, whereas the maximum conductivity occurs at intermediate water levels, ranging from approximately 0.5 to 1.5 water molecules per ion.

At low water levels, the interlayers are partially collapsed and poorly screened due to the segregation of water, severely constraining ionic motion. At high water levels (> 1.5 water molecules per ion), although the interlayer distance increases to $d_z \approx 6.8 \pm 0.1 \text{ \AA}$ and becomes spatially more uniform compared to the cases with less water, ionic mobility is again suppressed. In this regime, the reduced conductivity cannot be attributed to interlayer collapse; instead, it reflects a different microscopic mechanism (Figure 3).

At higher water levels (i.e., 1.5 water per ion or higher), water-poor regions vanish as most ions become fully solvated. We hypothesize that in this regime, water molecules occupy nearby octahedral sites that would otherwise serve as accessible hopping destinations for ions, thereby suppressing long-range ion motion (Figure 1b and Supplementary Movie X). Conversely, at very low water levels, ions are immobilized due to insufficient electrostatic screening and reduced interlayer spacing, which prevents hopping between neighboring octahedral sites. Notably, the water levels corresponding to maximum ionic conductivity coincide with the regime in which water-rich and water-poor 2D ionic domains largely coexist within the layers (Figure 2 and 3), suggesting a fine competition of aforementioned effects.

Trajectory analysis further confirms that in the absence of water and with high water levels, ions cannot move along the lattice. At intermediate water levels, where there is co-existence of water-poor and -rich regions, a visual inspection reveals that ions with little or no local hydration move over significantly longer distances than fully hydrated ions (Figure 3d and Supplementary movie X). Surprisingly, only ions residing near the boundary of water-poor zones contribute to directional ionic motion. At lower water levels (e.g., 0.2 water molecules per ion), extended water-poor ionic clusters span large regions of the layers, causing the interlayer spacing to approach the dehydrated limit locally (Supplementary Figure S3)

To further quantitatively assess the role of water in ion transport, we compute the displacement histograms of 2D ionic jump lengths along the field direction for each hydration level (Supplementary Figure S5). The distribution of ionic displacements Δx over time intervals of $\Delta t = 1$ ns, and 10 ns shows a pronounced asymmetry, particularly for $CN = 0$, at longer times under applied fields (Supplementary Figure S5). Calculating expected values and variances for jumps from these distributions reveals that jump lengths are minimal at both low and high water contents, consistent with negligible conductivity in these regimes (Figure 3d-e and Supplementary Figure S5). However, at intermediate water levels (i.e., one water per ion), ions exhibit longer jump distances on average and more extended individual ionic trajectories. In fact, ions with $CN = 0$ contribute disproportionately to ionic hops, while ions with $CN = 4$ exhibit the smallest hops (Figure 3e).

Taken together, these results demonstrate that ionic transport in intercalated MnO_2 layers requires a delicate balance: the interlayer spacing must exceed a critical threshold to permit hopping, while excessive hydration suppresses transport by blocking accessible hopping sites. Maximum ionic conductivity, therefore, emerges only in an intermediate hydration regime, where partial solvation enables electrostatic screening without eliminating available transport pathways.

Non-monotonic ionic conduction is due to an interplay of hydration and layer swelling

Our observation of a non-monotonic dependence of ionic current on intercalated water levels indicates the presence of two competing effects (Figure 3b). At high levels of interlayer water, water molecules hinder ion transport by occupying migration pathways and stabilizing ions in their octahedral sites, thereby suppressing hopping events, as previously reported in confined and layered systems.^{22,52,55} In contrast, at lower hydration levels, water plays a beneficial role by screening electrostatic interactions between ions and layer atoms, thereby expanding the interlayer spacing and facilitating the motion of partially or fully water-free ions.

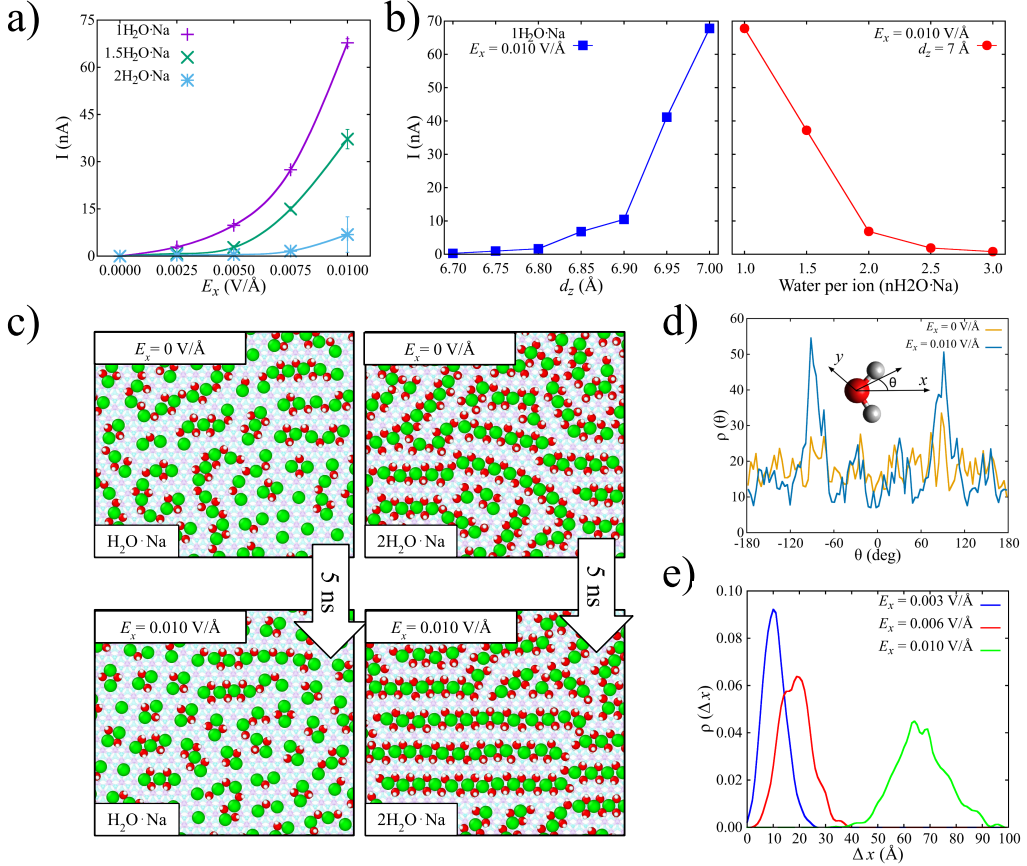


Figure 4: Ionic transport in rigid, fluctuation-free vdW layers. a) Applied electric field versus current for various water levels. b) Ionic current for (left) various interlayer distances at a fixed water level and (right) for various water levels at a fixed interlayer distance. c) Representative simulation snapshots demonstrating the ion and water distribution in a single layer ($d_z = 7$ Å) of MnO₂ at equilibrium and under an applied field of $E_x = 0.01$ V/Å. d) The distributions of the angle between the x axis and the water dipole on the xy plane. e) Displacement histograms of ions at $d_z = 7$ Å interlayer spacing for 10 ns-long simulations at various field strengths for 1H₂O·Na case.

To disentangle these two effects, we perform MD simulations in which the MnO_2 sheets are treated as rigid, static layers with a fixed interlayer spacing d_z . This frozen-layer approximation, commonly used in studies of confined electrolytes,^{5,16,41} eliminates morphological fluctuations of the host lattice and allows us to isolate the effects of interlayer spacing and hydration on ionic motion independently.^{56–58} Within this framework, we systematically vary the interlayer distance in separate simulations, while maintaining a fixed spacing and independently varying the water content.

We first set the water level to the value corresponding to maximum ionic conduction in unconstrained layers—namely, one water molecule per ion—and vary the interlayer spacing (Figure 3b). Under these conditions, measurable ionic motion occurs only when the nanosheet separation exceeds approximately $d_z \geq 6.0 \text{ \AA}$ (Figure 4b-c). Above this thickness, ionic conductivity increases monotonically with increasing interlayer spacing. Notably, unlike the deformable layers, the rigid layers do not exhibit an exponential increase in the ionic displacement, indicating the absence of solvent segregation (Supplementary Figure S6).

This confinement-induced suppression of mobility at small separations is consistent with trends reported for monovalent electrolytes confined between graphene sheets.¹⁶ These results also explain why, in unconstrained MnO_2 layers, gradual hydration enhances ionic conduction by expanding the interlayer distance and reducing confinement-induced barriers to ion hopping at moderate water levels (i.e., 1 water per ion in Figure 3).

Next, to isolate the role of water levels from the inter-layer thickness, we introduce controlled amounts of water—up to three water molecules per ion—between sodium-intercalated MnO_2 layers while maintaining a constant interlayer spacing of $d_z = 7.0 \text{ \AA}$ (Figure 4b-c). In equilibrium simulations without an external electric field, ions remain strongly bound to their initial octahedral sites, and thermal fluctuations alone are insufficient to induce hopping within the simulation timescale in these rigid layers (Supplementary Movie X). Upon the application of an external electric field, water-free systems exhibit zero ionic conduction up to an electric field-dependent threshold.

At nonzero water levels, less hydrated systems (e.g., one water molecule per ion) consistently exhibit higher ionic conductivity than more hydrated systems (two water molecules per ion) over a broad range of electric field strengths (Figure 4a). We attribute the reduced mobility at higher water contents to the formation of stable, 2D hydration shells: at two water molecules per ion, each ion is coordinated on average by four octahedrally bound water molecules, which strongly localize the ions and suppress their hopping (Figure 4 and Supplementary Figure S6). Representative simulation snapshots reveal that, under fixed interlayer spacing, ions organize into filamentous clusters aligned along the field direction (Figure 4c). At high water levels, these ion “trains” are highly ordered, where water dipoles are aligned perpendicular to the field direction to stabilize these trains (Figure 4b,e). These well-hydrated ion trains display minimal motion despite drifting collectively in the field direction, resulting in negligible net displacement and low conductivity (Supplementary Movie X). Correspondingly, the average ion–ion distance decreases under applied fields in the highly hydrated case, indicating enhanced electrostatic screening that promotes clustering (Supplementary Figure S6). We repeat simulations with extended lateral dimensions and observe the same filamentous cluster formation patterns. At sufficiently strong electric fields (i.e., $E_x \gtrsim 0.01$ V/Å), the clusters span the entire simulation box along the field direction (Supplementary Figure S6), indicating that their growth is not an artifact of system size (Supplementary Figure S6).

In contrast, at lower water levels, some octahedral sites remain unoccupied by water, providing accessible hopping destinations for ions. Under these conditions, cluster formation is weaker, structural ordering is reduced, and ionic mobility is enhanced (Figure 4). Importantly, the field-induced alignment of ions with water molecules persists even at larger interlayer separations in rigid, fluctuation-free layers (Supplementary Figure S7),

Overall, simulations performed under a constant interlayer spacing with varying water levels confirm two opposing mechanisms governing ionic transport in MnO_2 layers. Interlayer expansion promotes conduction by reducing confinement and electrostatic binding, while

excessive hydration suppresses conduction by stabilizing ions in water-coordinated clusters that block hopping pathways. The formation of finite-size water-rich and water-poor domains favors the optimum thickness and hydration levels for ionic motion. The competition between these effects naturally explains the experimentally observed non-monotonic dependence of ionic conductivity on hydration level.

Conclusion

Water plays a dual and indispensable role in stabilizing ion-intercalated MnO_2 vdW-layered structures and enabling ionic transport within vdW layered structures. In the absence of interlayer water, MnO_2 sheets collapse, are distorted, and lose ionic conductivity, consistent with prior experimental and theoretical studies.^{19,22,59} Negatively charged MnO_2 surfaces strongly interact with confined water molecules, orienting their dipoles and disrupting the bulk hydrogen-bond network,⁶⁰ while simultaneously regulating the interlayer spacing that governs ionic mobility.

In this work, inspired by previous experimental findings, we combined non-equilibrium all-atom MD simulations to elucidate the mechanisms governing field–driven ion transport in monovalent-ion-intercalated MnO_2 layers. Our results demonstrate that ionic conduction arises from a subtle interplay between ion hydration, electrostatic screening, and the water-mediated morphology of the confining vdW layers. Water molecules stabilize Na^+ ions by forming hydration shells, which can suppress ionic hopping, in agreement with previous studies of confined electrolytes.⁶¹ In simulations employing rigid, fluctuation-free MnO_2 sheets, reducing hydration monotonically enhances ionic mobility by exposing octahedral hopping sites and lowering steric constraints (Figure 4). However, this trend contradicts previous experimental observations, which showed suppressed conductivity at high vacuum or elevated temperatures, where interlayer water is depleted.^{15,19}

When MnO_2 sheets are allowed to deform in response to local water levels, water becomes

essential for stabilizing the layered morphology and preventing the formation of current-dead regions. Our simulations reveal that electric fields induce spatial segregation of water into water-rich and water-poor domains, leading to nanoscopic regions occupied by hydrated and unhydrated ions, respectively. This segregation also results in a hydration-dependent interlayer spacing and heterogeneous ionic transport pathways (Figure 2 and 3). Specifically, ions located at the boundaries of these domains contribute most to conduction, while fully water-stripped or fully hydrated ions are minimally mobilized by the external field. If boundary regions percolate across the layered crystal, ionic conduction is sustained; if not, conductivity can vanish entirely. Consequently, we observe a monotonic decrease in ionic conductivity with increasing water levels, consistent with experimental measurements on micron-scale MnO_2 crystallites (Figures 3 and 4).

Notably, although field-induced segregation occurs in both rigid and flexible layers, it leads to markedly higher ionic currents in rigid systems. This contrast highlights the essential role of surface morphology. Surface oscillations have previously been shown to strongly influence molecular friction and water transport.^{58,62} Our simulations also demonstrate that the absence of surface oscillations lowers the energy barriers for collective ion hopping, thereby enhancing conductivity. Thus, surface dynamics emerge as a key control parameter for optimizing ionic transport in ion-intercalated layered materials.

Finally, stacked MnO_2 layers exhibit strong dielectric anisotropy, characterized by high in-plane and low out-of-plane permittivity.^{63–65} This rapid screening along the confinement direction effectively decouples adjacent layers, amplifying the influence of local morphology and hydration on ionic motion. Taken together, our results establish that ionic conduction in MnO_2 vdW layers is governed not solely by ion hydration or confinement, but by their collective coupling to dynamic surface morphology and electrostatic correlations. These insights provide a framework for rationally tuning ionic transport in layered oxides and open avenues for designing voltage-controlled ionic devices based on ion-intercalated vdW structures.

Acknowledgement

The numerical calculations reported in this paper were partially performed at TUBITAK ULAKBIM, High Performance and Grid Computing Center (TRUBA resources). AUO acknowledges the TUBITAK 124N935 and TUBITAK National PhD Scholarship Program 2211.

References

- (1) Watanabe, M.; Thomas, M. L.; Zhang, S.; Ueno, K.; Yasuda, T.; Dokko, K. Application of Ionic Liquids to Energy Storage and Conversion Materials and Devices. *Chemical Reviews* **2017**, *117*, 7190–7239, PMID: 28084733.
- (2) Joshi, A.; Mishra, D. K.; Singh, R.; Zhang, J.; Ding, Y. A comprehensive review of solid-state batteries. *Applied Energy* **2025**, *386*, 125546.
- (3) Kulathuvayal, A. S.; Su, Y. Ionic Transport through the Solid Electrolyte Interphase in Lithium-Ion Batteries: A Review from First-Principles Perspectives. *ACS Applied Energy Materials* **2023**, *6*, 5628–5645.
- (4) Zhou, W.; Zhang, M.; Kong, X.; Huang, W.; Zhang, Q. Recent Advance in Ionic-Liquid-Based Electrolytes for Rechargeable Metal-Ion Batteries. *Advanced Science* **2021**, *8*, 2004490.
- (5) Robin, P.; Kavokine, N.; Bocquet, L. Modeling of emergent memory and voltage spiking in ionic transport through angstrom-scale slits. *Science* **2021**, *373*, 687–691.
- (6) Zhang, H.; Li, J.; Liu, J.; Gao, Y.; Fan, Y.; Liu, X.; Guo, C.; Liu, H.; Chen, X.; Wu, X.; Liu, Y.; Gu, Q.; Li, L.; Wang, J.; Chou, S.-L. Understanding capacity fading from structural degradation in Prussian blue analogues for wide-temperature sodium-ion cylindrical battery. *Nature Communications* **2025**, *16*, 2520.

(7) Zhang, S. Chemomechanical modeling of lithiation-induced failure in high-volume-change electrode materials. *npj Computational Materials* **2017**, *3*, 7, Modeling stress, fracture, and degradation due to repeated lithiation cycles.

(8) Radha, B. et al. Molecular transport through capillaries made with atomic-scale precision. *Nature* **2016**, *538*, 222–225.

(9) Yang, R.; Mei, L.; Lin, Z.; Fan, Y.; Lim, J.; Guo, J.; Liu, Y.; Shin, H. S.; Voiry, D.; Lu, Q.; Li, J.; Zeng, Z. Intercalation in 2D materials and in situ studies. *Nature Reviews Chemistry* **2024**, *8*, 410–432.

(10) Zou, Y.-C. et al. Ion exchange in atomically thin clays and micas. *Nature Materials* **2021**, *20*, 1677–1682.

(11) Zhou, J.; Lin, Z.; Ren, H.; Duan, X.; Shakir, I.; Huang, Y.; Duan, X. Layered Intercalation Materials. *Advanced Materials* **2021**, *33*, 2004557.

(12) Noh, G. et al. Electrolyte-free potassium ions intercalated in 2D layered metal oxide for imitating spatiotemporal biological neural dynamics. *Materials Today* **2025**, *85*, 27–38.

(13) Rajapakse, M.; Karki, B.; Abu, U. O.; Pishgar, S.; Musa, M. R. K.; Riyadh, S. M. S.; Yu, M.; Sumanasekera, G.; Jasinski, J. B. Intercalation as a versatile tool for fabrication, property tuning, and phase transitions in 2D materials. *npj 2D Materials and Applications* **2021**, *5*, 30.

(14) Wu, Y.; Li, D.; Wu, C.-L.; Hwang, H. Y.; Cui, Y. Electrostatic gating and intercalation in 2D materials. *Nature Reviews Materials* **2023**, *8*, 41–53.

(15) Rasouli, H. R.; Kim, J.; Mehmood, N.; Sheraz, A.; Jo, M.-k.; Song, S.; Kang, K.; Kasirga, T. S. Electric-Field-Induced Reversible Phase Transitions in a Spontaneously Ion-Intercalated 2D Metal Oxide. *Nano Letters* **2021**, *21*, 3997–4005, PMID: 33881885.

(16) Fong, K. D.; Grey, C. P.; Michaelides, A. On the Physical Origins of Reduced Ionic Conductivity in Nanoconfined Electrolytes. *ACS Nano* **2025**, *19*, 13191–13201, PMID: 40130707.

(17) Kong, J.; Bo, Z.; Yang, H.; Yang, J.; Shuai, X.; Yan, J.; Cen, K. Temperature dependence of ion diffusion coefficients in NaCl electrolyte confined within graphene nanochannels. *Phys. Chem. Chem. Phys.* **2017**, *19*, 7678–7688.

(18) Dockal, J.; Moučka, F.; Lísal, M. Molecular Dynamics of Graphene-Electrolyte Interface: Interfacial Solution Structure and Molecular Diffusion. *The Journal of Physical Chemistry C* **2019**, *2019*.

(19) Parsi, A.; Suleiman, A. A.; Razeghi, M.; Pehlivanoglu, D.; Oğuz, O.; Başçı, U.; Shakir, H. M.; Yegin, E.; Kasirga, T. S. Synthesis of intrinsically sodium intercalated ultra-thin layered MnO₂ and its ionic charge transport. *Nanoscale* **2025**, *17*, 9337–9345.

(20) Nam, K. W. et al. The High Performance of Crystal Water Containing Manganese Birnessite Cathodes for Magnesium Batteries. *Nano Letters* **2015**, *15*, 4071–4079, PMID: 25985060.

(21) Post, J. E. Manganese oxide minerals: Crystal structures and economic and environmental significance. *Proceedings of the National Academy of Sciences* **1999**, *96*, 3447–3454.

(22) Shan, X.; Guo, F.; Charles, D. S.; Lebens-Higgins, Z.; Abdel Razek, S.; Wu, J.; Xu, W.; Yang, W.; Page, K. L.; Neufeld, J. C.; et al. Structural water and disordered structure promote aqueous sodium-ion energy storage in sodium-birnessite. *Nature Communications* **2019**, *10*.

(23) Yin, B.; Zhang, S.; Jiang, H.; Qu, F.; Wu, X. Phase-controlled synthesis of polymorphic MnO₂ structures for electrochemical energy storage. *J. Mater. Chem. A* **2015**, *3*, 5722–5729.

(24) Devi, R.; Kumar, V.; Kumar, S.; Bulla, M.; Sharma, S.; Sharma, A. Electrochemical Analysis of MnO_2 (α , β , and γ)-Based Electrode for High-Performance Supercapacitor Application. *Applied Sciences* **2023**, *13*.

(25) Pan, Y.; Jiawei, W.; Haifeng, W.; Song, W.; Chunyuan, Y.; Yue, H. Physicochemical properties of different crystal forms of manganese dioxide prepared by a liquid phase method and their quantitative evaluation in capacitor and battery materials. *Nanoscale Adv.* **2023**, *5*, 3396–3413.

(26) Zhu, X.; Xu, J.; Zhang, Q.; Shen, T.; Zhuang, Y.; Chen, T.; Li, S.; Gu, L.; Xia, H. Regulating Na content and Mn defects in birnessite for high-voltage aqueous sodium-ion batteries. *Nature Communications* **2025**, *16*, 3838.

(27) Sau, K.; Takagi, S.; Ikeshoji, T.; Kisu, K.; Sato, R.; dos Santos, E. C.; Li, H.; Mohtadi, R.; Orimo, S.-i. Unlocking the secrets of Ideal Fast Ion conductors for all-solid-state batteries. *Communications Materials* **2024**, *5*.

(28) Jamnik, J.; Maier, J.; Pejovnik, S. Interfaces in solid ionic conductors: Equilibrium and small signal picture. *Solid State Ionics* **1995**, *75*, 51–58.

(29) Lopano, C. L.; Heaney, P. J.; Bandstra, J. Z.; Post, J. E.; Brantley, S. L. Kinetic analysis of cation exchange in birnessite using time-resolved synchrotron X-ray diffraction. *Geochimica et Cosmochimica Acta* **2011**, *75*, 3973–3981.

(30) Mang, C.; Luo, J.; Cao, P.; Zhang, X.; Rao, M.; Li, G.; Jiang, T. Importance of water content in birnessite-type MnO_2 catalysts for HCHO oxidation: Mechanistic details and DFT analysis. *Chemosphere* **2022**, *287*, 132293.

(31) Boyd, S.; Ganeshan, K.; Tsai, W.-Y.; Tao, W.; Saeed, S.; Jiang, D.-e.; Balke, N.; van Duin, A.; Augustyn, V. Effects of interlayer confinement and hydration on capacitive charge storage in birnessite. *Nature Materials* **2021**, *20*.

(32) Wang, C.; Xu, B.; Zhang, X.; Sun, W.; Chen, J.; Pan, H.; Yan, M.; Jiang, Y. Ion Hopping: Design Principles for Strategies to Improve Ionic Conductivity for Inorganic Solid Electrolytes. *Small* **2022**, *18*.

(33) Hou, T.; Xu, W.; Pei, X.; Jiang, L.; Yaghi, O. M.; Persson, K. A. Ionic Conduction Mechanism and Design of Metal–Organic Framework Based Quasi-Solid-State Electrolytes. *Journal of the American Chemical Society* **2022**, *144*, 13446–13450, PMID: 35700972.

(34) Kwon, K. D.; Refson, K.; Sposito, G. Understanding the trends in transition metal sorption by vacancy sites in birnessite. *Geochimica et Cosmochimica Acta* **2013**, *101*, 222–232.

(35) Han, S.; Kwon, K. D. Interlayer water structure of phyllosilicate minerals: Insights from MD simulations of chalcophanite-group oxide dehydration. *Geochimica et Cosmochimica Acta* **2022**, *318*, 495–509.

(36) Chen, D.; Ding, D.; Li, X.; Waller, G. H.; Xiong, X.; El-Sayed, M. A.; Liu, M. Probing the Charge Storage Mechanism of a Pseudocapacitive MnO₂ Electrode Using in Operando Raman Spectroscopy. *Chemistry of Materials* **2015**, *27*, 6608–6619.

(37) He, Q.; Yu, B.; Li, Z.; Zhao, Y. Density Functional Theory for Battery Materials. *ENERGY & ENVIRONMENTAL MATERIALS* **2019**, *2*, 264–279.

(38) Stacy, E.; Gainaru, C.; Gobet, M.; Wojnarowska, Z.; Bocharova, V.; Greenbaum, S.; Sokolov, A. Fundamental Limitations of Ionic Conductivity in Polymerized Ionic Liquids. *Macromolecules* **2018**, *51*.

(39) Luong, N. T.; Oderstad, H.; Holmboe, M.; Boily, J.-F. Temperature-resolved nanoscale hydration of a layered manganese oxide. *Phys. Chem. Chem. Phys.* **2023**, *25*, 17352–17359.

(40) Toquer, D.; Bocquet, L.; Robin, P. Ionic association and Wien effect in 2D confined electrolytes. *The Journal of Chemical Physics* **2025**, *162*, 064703.

(41) Jiménez-Ángeles, F.; Ehlen, A.; Olvera de la Cruz, M. Surface polarization enhances ionic transport and correlations in electrolyte solutions nanoconfined by conductors. *Faraday Discuss.* **2023**, *246*, 576–591.

(42) Lopano, C.; Heaney, P.; Post, J.; Brantley, S. Determination of cation exchange rates in synthetic birnessite using time-resolved synchrotron X-ray diffraction. *Geochimica et Cosmochimica Acta Supplement* **2005**,

(43) Cygan, R. T.; Greathouse, J. A.; Kalinichev, A. G. Advances in Clayff Molecular Simulation of Layered and Nanoporous Materials and Their Aqueous Interfaces. *The Journal of Physical Chemistry C* **2021**, *125*, 17573–17589.

(44) Newton, A. G.; Kwon, K. D. Classical mechanical simulations of layer- and tunnel-structured manganese oxide minerals. *Geochimica et Cosmochimica Acta* **2020**, *291*, 92–109, Multiscale Simulation in Geochemistry.

(45) Newton, A. G.; Kwon, K. D. Molecular simulations of hydrated phyllo manganeseates. *Geochimica et Cosmochimica Acta* **2018**, *235*, 208–223.

(46) Hockney, R. W.; Eastwood, J. W. *Computer simulation using particles*; 1988.

(47) Ryckaert, J.-P.; Ciccotti, G.; Berendsen, H. J. Numerical integration of the cartesian equations of motion of a system with constraints: molecular dynamics of n-alkanes. *Journal of Computational Physics* **1977**, *23*, 327–341.

(48) Martínez, L.; Andrade, R.; Birgin, E.; Martínez, J. M. PACKMOL: A package for building initial configurations for molecular dynamics simulations. *Journal of Computational Chemistry* **2009**, *30*, 2157 – 2164.

(49) Parrinello, M.; Rahman, A. Polymorphic transitions in single crystals: A new molecular dynamics method. *Journal of Applied Physics* **1981**, *52*, 7182–7190.

(50) Tuckerman, M. E.; Alejandre, J.; López-Rendón, R.; Jochim, A. L.; Martyna, G. J. A Liouville-operator derived measure-preserving integrator for molecular dynamics simulations in the isothermal–isobaric ensemble. *Journal of Physics A: Mathematical and General* **2006**, *39*, 5629.

(51) Shinoda, W.; Shiga, M.; Mikami, M. Rapid estimation of elastic constants by molecular dynamics simulation under constant stress. *Phys. Rev. B* **2004**, *69*, 134103.

(52) Cheng, W.; Lindholm, J.; Holmboe, M.; Luong, N. T.; Shchukarev, A.; Ilton, E. S.; Hanna, K.; Boily, J.-F. Nanoscale Hydration in Layered Manganese Oxides. *Langmuir* **2021**, *37*, 666–674, PMID: 33404244.

(53) André, E.; Cornu, D.; Pérez Ramírez, L.; Durand, P.; Gallet, J.-J.; Bournel, F.; Röchet, F.; Ruby, C.; Carteret, C.; Coustel, R. The dehydration mechanism of Na and K birnessites: a comprehensive multitechnique study. *Dalton Trans.* **2024**, *53*, 9952–9963.

(54) Cygan, R. T.; Post, J. E.; Heaney, P. J.; Kubicki, J. D. Molecular models of birnessite and related hydrated layered minerals. *American Mineralogist* **2012**, *97*, 1505–1514.

(55) Yoshisako, H.; Okamoto, N. L.; Tanaka, K.; Ichitsubo, T. Utilizing surface water adsorption on layered MnO₂ nanosheets for enhancing heat storage performance. *Communications Chemistry* **2025**, *8*, 169.

(56) Shan, X.; Pidathala, R. T.; Kim, S.; Xu, W.; Abeykoon, M.; Kwon, G.; Olds, D.; Narayanan, B.; Teng, X. Exemption of lattice collapse in Ni–MnO₂ birnessite regulated by the structural water mobility. *J. Mater. Chem. A* **2021**, *9*, 23459–23466.

(57) Ma, M.; Grey, F.; Shen, L.; Urbakh, M.; Wu, S.; Liu, J. Z.; Liu, Y.; Zheng, Q. Water

transport inside carbon nanotubes mediated by phonon-induced oscillating friction. *Nature Nanotechnology* **2015**, *10*, 692–695.

(58) Erbaş, A.; Horinek, D.; Netz, R. R. Viscous Friction of Hydrogen-Bonded Matter. *Journal of the American Chemical Society* **2012**, *134*, 623–630, PMID: 22098642.

(59) Johnson, E. A.; Post, J. E. Water in the interlayer region of birnessite: Importance in cation exchange and structural stability. *American Mineralogist* **2006**, *91*, 609–618.

(60) Remsing, R. C.; McKendry, I. G.; Strongin, D. R.; Klein, M. L.; Zdilla, M. J. Frustrated Solvation Structures Can Enhance Electron Transfer Rates. *The Journal of Physical Chemistry Letters* **2015**, *6*, 4804–4808, PMID: 26573339.

(61) Li, Y.; Yu, Y.; Qian, J.; Wu, H.; Wang, F. Anomalous ion transport through angstrom-scale pores: Effect of hydration shell exchange on ion mobility. *Applied Surface Science* **2021**, *560*, 150022.

(62) Bocquet, L.; Netz, R. R. Phonon modes for faster flow. *Nature Nanotechnology* **2015**, *10*, 657–658.

(63) Frisenda, R.; Niu, Y.; Gant, P.; Muñoz, M.; Castellanos-Gomez, A. Naturally occurring van der Waals materials. **2020**,

(64) Arias, N. P.; Becerra, M. E.; Giraldo, O. Structural and Electrical Studies for Birnessite-Type Materials Synthesized by Solid-State Reactions. *Nanomaterials* **2019**, *9*.

(65) Moreira, A. G.; Netz, R. R. Binding of Similarly Charged Plates with Counterions Only. *Phys. Rev. Lett.* **2001**, *87*, 078301.

Supplementary Information: Ionic transport in spontaneously ion-intercalated van der Waals layered structures

Ata Utku Özkan,^{*,†,¶} T. Serkan Kasırga,^{*,‡,¶} and Aykut Erbaş^{*,†,¶}

[†]Institute of Materials Science and Nanotechnology, Bilkent University, Ankara 06800, Turkiye

[‡]Department of Physics, Middle East Technical University, Ankara 06800, Turkiye

[¶]Bilkent National Nanotechnology Research Center - UNAM, Ankara 06800, Turkiye

E-mail: utku.ozkan@bilkent.edu.tr; kasirga@unam.bilkent.edu.tr;
aykut.erbas@unam.bilkent.edu.tr

MnO parameters:

Element	Charge(e)	D_θ (kcal/mol)	R_θ (Å)
Mn	1.85	9.0298e-07	5.5070
O	-1.05	0.1554	3.5532
Na	1	0.1301	2.6378

Water parameters:

Element	Charge(e)	D_θ (kcal/mol)	R_θ (Å)
O	-0.8476	0.1554	3.5532
H	0.4238	-	-

Bond type	k (kcal/mol Å ²)	r_0 (Å)
O-H	554.1349	1.0000

Angle	k (kcal/mol rad ²)	θ_0 (deg)
H-O-H	45.7696	109.47

TABLE S1: CLAYFF force-field parameters.¹⁻³

E_x	τ (ns)	$\langle v_x \rangle$ (Å/ns)	c_1	c_2	$\langle v_l \rangle$ (Å/ns)	b
0.010	13.2650	0.0055	0.6775	0.2868	0.0062	0.9086
0.015	14.1710	0.0112	2.0343	0.6951	0.0138	2.5089
0.020	16.3553	0.0225	3.1662	1.3233	0.0278	4.0323
0.025	15.5962	0.0312	8.4501	1.3891	0.0391	8.6612

TABLE S2: Displacement curve fit parameters. The equation used to fit displacement curves for $1\text{H}_2\text{O}\cdot\text{Na}$ is given by $\Delta x = c_1(1 - \exp(-t/\tau)) + \langle v_t \rangle t + c_2$, where c_1 and c_2 are fitting constants associated with the initial response and offset, τ is the relaxation timescale, above which a linear increase in the displacement data is observed and $\langle v_t \rangle$ is the steady state ion velocity. As a consistency check, we also fit only the steady state (50–100 ns) with $\Delta x = \langle v_t \rangle t + b$ and report those parameters.

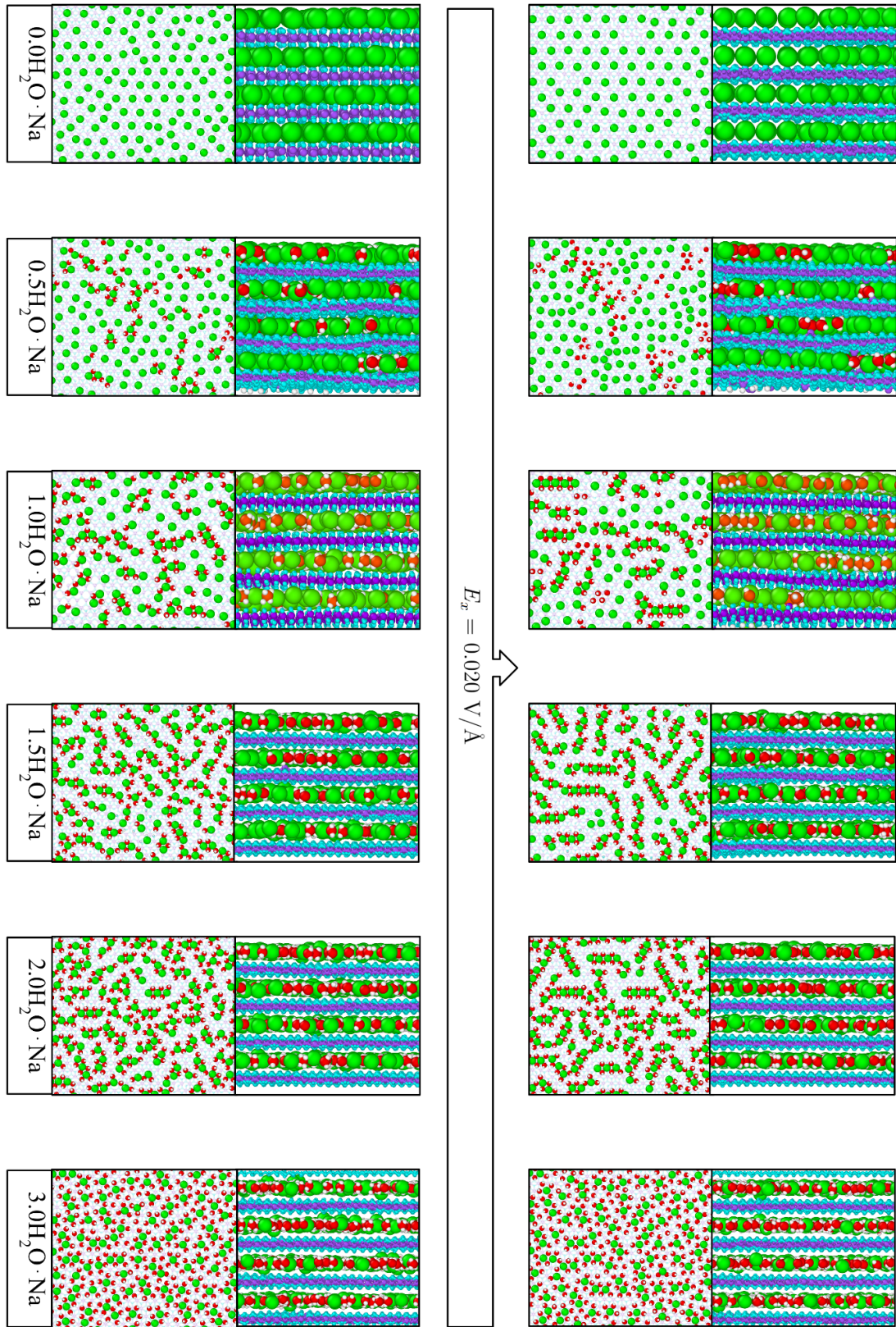


FIGURE S1: Interlayer conformations of systems in different water concentrations at equilibrium and after 50 ns under the applied field of $E_x = 0.020 \text{ V/}\text{\AA}$.

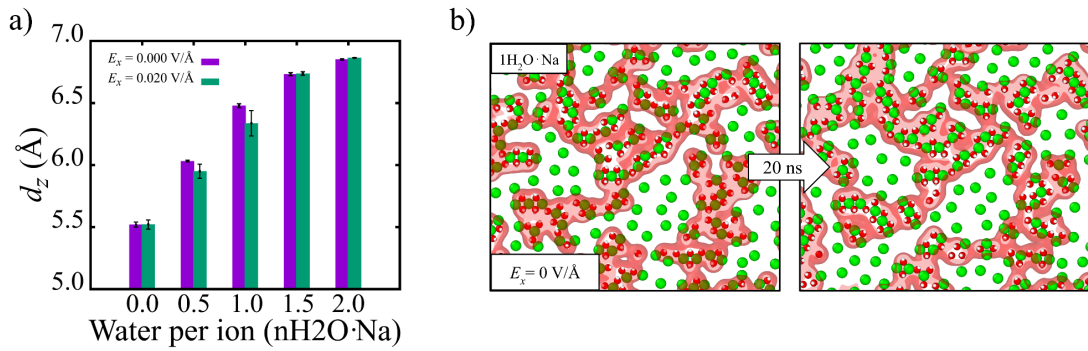


FIGURE S2: (a) Interlayer spacing before and after application of an external electric field for different water concentrations. (b) Non-spontaneously rehomogenizing system exhibiting a non-uniform initial water distribution where water molecules are initially distributed non-uniformly and equilibrated in the absence of an external electric field for 20 ns. Water molecules are enclosed by a surface mesh to improve visual clarity.

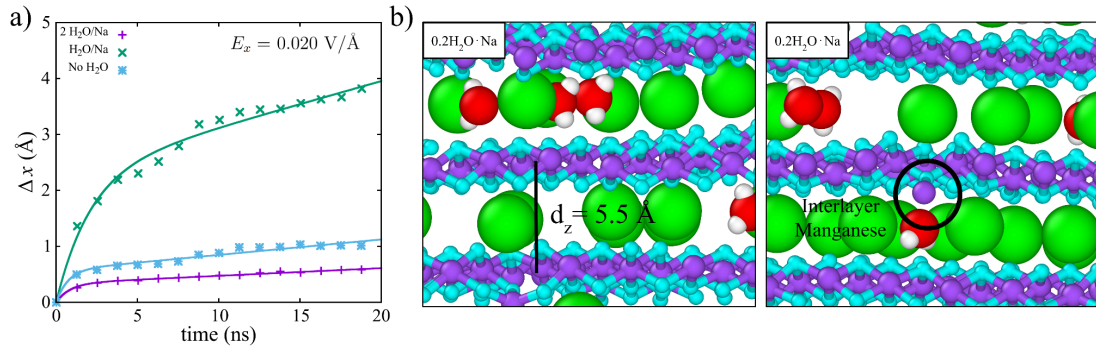


FIGURE S3: (a) Displacement trajectories for high- and low-hydration systems, along with (b) low-hydration snapshots illustrating local interlayer collapse and manganese migration into the interlayer region.

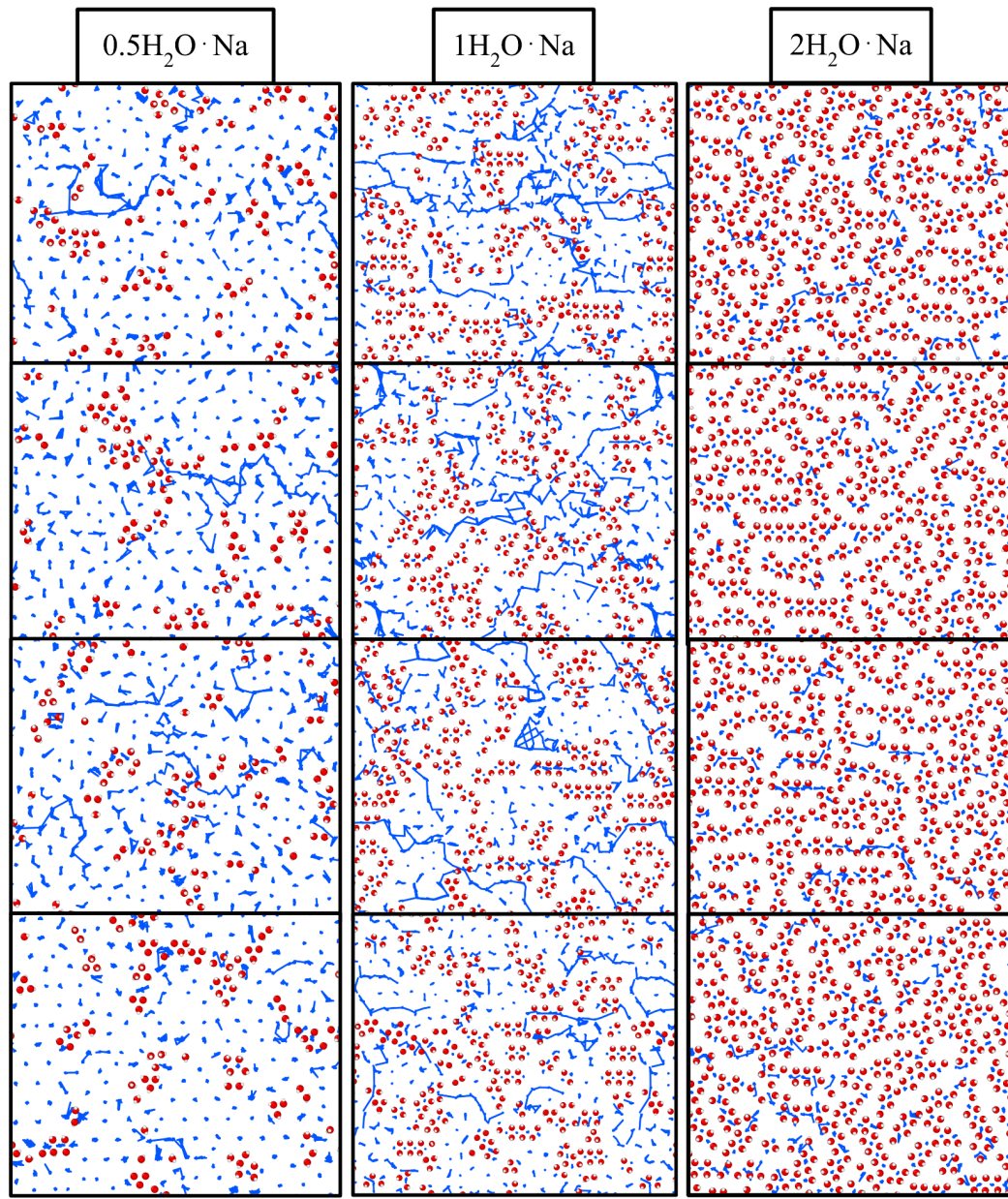


FIGURE S4: 50 ns displacement trajectory of sodium ions under different water concentrations with $E_x = 0.020$ V/Å. These trajectories are drawn from the second half of the simulation (50-100 ns), thus do not show the initial redistribution of ions. Blue lines indicate ion movements. Ions are not shown for clarity.

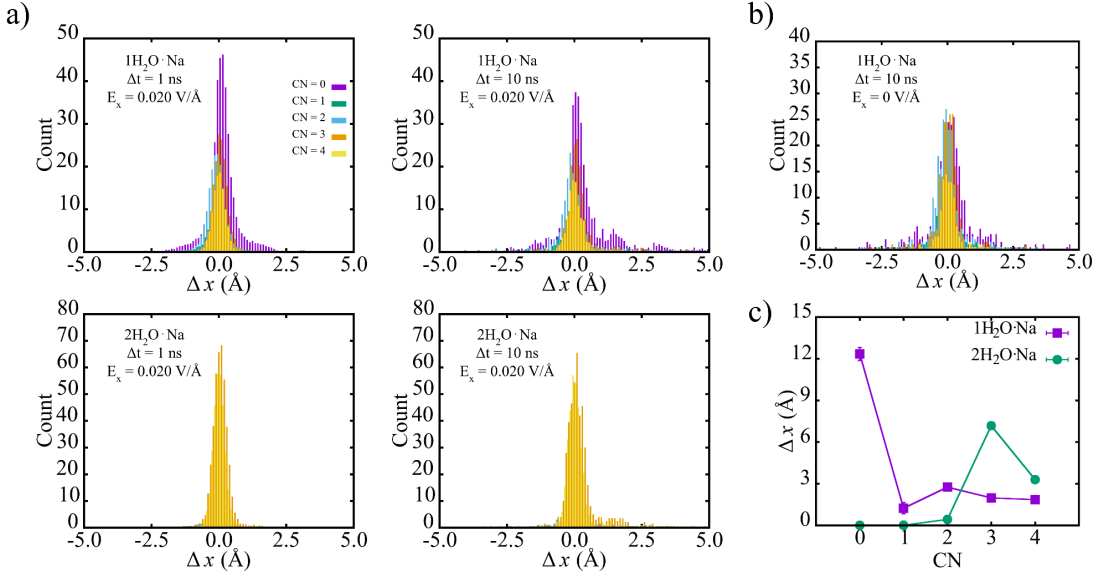


FIGURE S5: (a) Displacement histograms of $1\text{H}_2\text{O}\cdot\text{Na}$ and $2\text{H}_2\text{O}\cdot\text{Na}$ systems binned with different time windows. Ions with the same coordination number (CN) are selected at time t , and their displacements are evaluated relative to the configuration at $t+\Delta t$, without imposing conservation of the coordination number between the two frames. Then the displacement values are binned for each CN and averaged over the total number of timeframes. (b) Displacement histograms of the $1\text{H}_2\text{O}\cdot\text{Na}$ system without an applied electric field. (c) Coordination number versus average ionic displacement in 50 ns simulations under an applied field of $E_x = 0.020\text{ V}/\text{\AA}$.

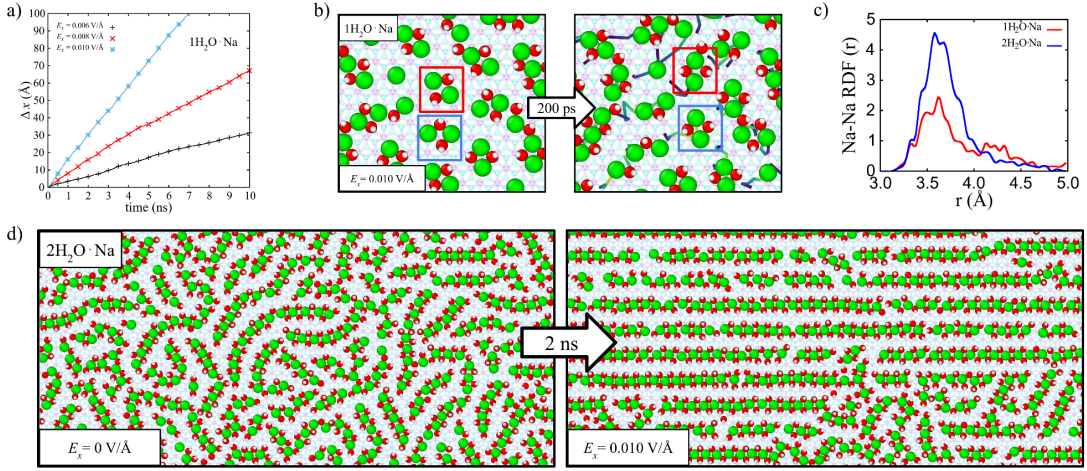


FIGURE S6: (a) Displacement trajectories for rigid layer $1\text{H}_2\text{O}\cdot\text{Na}$ systems under various electric fields. (b) Snapshots illustrating the ionic hopping mechanism in rigid-layer $1\text{H}_2\text{O}\cdot\text{Na}$ systems, showing ion migration between neighboring octahedral sites. (c) Sodium-Sodium (Na-Na) radial distribution functions of 1 and $2\text{H}_2\text{O}\cdot\text{Na}$ systems without an applied electric field. (d) Snapshots (2x1x1 system) of organization of filamentous clusters along field direction in $2\text{H}_2\text{O}\cdot\text{Na}$ rigid layer system.

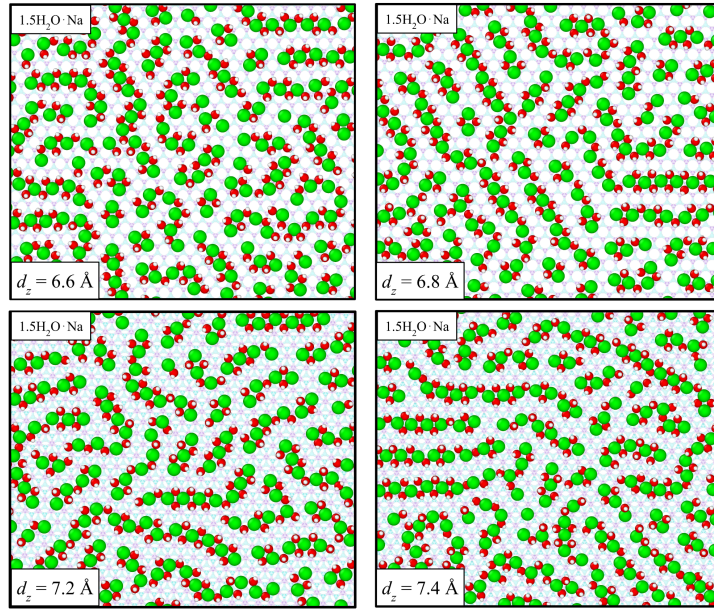


FIGURE S7: Snapshots of rigid layer $1.5\text{H}_2\text{O}\cdot\text{Na}$ systems equilibrated without an applied electric field in various interlayer distances demonstrating different sizes of clusters.

References

- [1] Cygan, R. T.; Greathouse, J. A.; Kalinichev, A. G. Advances in Clayff Molecular Simulation of Layered and Nanoporous Materials and Their Aqueous Interfaces. *The Journal of Physical Chemistry C* 2021, 125, 17573–17589
- [2] Newton, A. G.; Kwon, K. D. Classical mechanical simulations of layer- and tunnel structured manganese oxide minerals. *Geochimica et Cosmochimica Acta* 2020, 291, 92–109, Multiscale Simulation in Geochemistry.
- [3] Newton, A. G.; Kwon, K. D. Molecular simulations of hydrated phyllosilicates. *Geochimica et Cosmochimica Acta* 2018, 235, 208–223.